Classical theory for asymmetric in-plane atom surface scattering

Eli Pollak* and Jeremy M. Moix
Chemical Physics Department, Weizmann Institute of Science, 76100 Rehovoth, Israel

Salvador Miret-Artés
Instituto de Física Fundamental, Consejo Superior de Investigaciones Científicas, Serrano 123, 28006 Madrid, Spain
(Received 25 May 2009; revised manuscript received 24 August 2009; published 21 October 2009)

In-plane atom surface scattering perturbation theory within a generalized Langevin equation formalism is proposed to account for the asymmetry found in angular distributions of heavy rare gas atoms scattered by corrugated surfaces. We show that when the surface corrugation is represented in terms of the first two (sine) Fourier components, one finds an asymmetric angular distribution. This asymmetry reflects the ratchetlike form of the effective corrugation. Adding in higher-order terms can also increase the number of rainbow scattering angles. Three rainbows are found for a second-order sine term in the corrugation, four symmetrically spaced rainbow angles are found when adding in a second-order cosine term to the corrugation. Analytic expressions for the angular distribution are derived in terms of a Morse oscillator model. The theory accounts well for the asymmetry and predicts its disappearance as the incident scattering angle is increased. It also features a decrease in the distance between the rainbow angles as the angle of incidence is increased and as the incident energy is increased. The theory is successfully applied to the experimental results of Kondo *et al.* [Eur. Phys. J. D **38**, 129 (2006)] for the scattering of Ar on LiF(100) and the results of Amirav *et al.* [J. Chem. Phys. **87**, 1796 (1987)] for the scattering of Xe on Ge(100) and Ar and Kr on Ag(100).

DOI: 10.1103/PhysRevB.80.165420 PACS number(s): 34.35.+a, 34.50.−s, 61.05.Np, 68.49.Bc

I. INTRODUCTION

During the past fifty years a large body of experimental data has been amassed about the scattering of atoms on surfaces. Much of the work was concentrated on light atom scattering such as He[1–6] due to the interest in quantum diffraction,[7,8] selective adsorption resonances,[9,10] and phonon dispersion curves. However, many heavy atom systems have also been studied, including heavy rare gases such as Ar (Refs. 11–29) and Xe.[30–37] For these, a classical theory of scattering is appropriate. If one neglects the interaction with surface phonons and one assumes that the scattering potential in the horizontal direction is a single cosine or sine term, then theory predicts that the angular distribution will be symmetrically displaced about the specular scattering angle.[38–42] If rainbow scattering is important then one will observe two symmetrically displaced peaks about the specular angle, which is now a minimum in the angular distribution. If the broadening induced by surface phonons is larger than the spacing between the rainbow angles then the distribution should be symmetrically centered with a maximum at the specular angle.[43,44] This may occur as a result of phonons or disorder, for example, when scattering from a liquid.[45]

Although this simplistic picture is valid as a zeroth-order approximation, theory, experiments, and numerical simulations provide a richer picture. In many cases, the angular distribution is somewhat shifted usually to superspecular angles. This is the case for example for the scattering of Ar on an Ag(111) surface where the angular distributions are shifted to superspecular angles.[23] Similarly, in the scattering of Ar on a Ir(110) surface[15] or Ne on an Au(110) surface, in the $[1\bar{1}0]$ azimuth, one finds that the peak in the angular distribution is superspecular. The first observation of rainbow scattering was for the scattering of Ne on LiF(001), showing an asymmetric double peaked distribution.[46] Rainbow scattering and strong asymmetry are also observed when Ne is scattered along the [001] azimuth[47] of Au(110). Asymmetric rainbow scattering has been observed for the scattering of Ar from Cu(110).[12] More recent work on the scattering of Ar on a Ru(0001) surface exhibits a bell-shaped angular distribution, which is superspecular when the incident angle is 50°. When the scattering energy is 0.56 eV and the incident angle is 60°, one observes asymmetric rainbow scattering.[25] When Xe is scattered from a Pt(111) surface one observes superspecular scattering over a broad range of incidence energies.[32]

There are a variety of reasons for observing angular distributions which differ from the simplistic picture. In the derivation of the washboard model, Tully[38] noted that when the angle of incidence is not zero the approaching particle may be exposed to an asymmetric corrugation since the particle has a larger probability of striking a region where the surface slopes toward the incoming particle. This asymmetry leads to an asymmetric angular distribution.

Especially at large incidence angles or low energies, the projectile may be partially trapped in the physisorption well. It then desorbs statistically and so contributes a broad background to the part of the distribution, which is directly scattered. Even when the scattering is direct, in the sense that the atom comes in and immediately goes out, one may observe a shift in the location of the maximum of the peak. As shown in our recent studies,[41,42] the shift may be induced through the inelastic interaction with the surface. If the friction felt by the particle is larger along the horizontal direction than the vertical, the momentum in the horizontal direction is reduced more than the vertical and so one should observe subspecular scattering. Conversely, if the friction along the vertical direction is larger, as is usually the case when the vertical energy is not too small, then the momentum loss in

the vertical direction is large and one should observe superspecular scattering. However, this argument does not suffice to explain the superspecular scattering in a system such as Ar on Ag(111), where the shift seems to be constant over a very large range of energies.[23] Moreover, we are not aware of a simple theoretical analysis which explains the strong asymmetry observed especially when rainbow scattering is important. This is the central issue of this paper.

In most simplified models of the scattering,[38–40] as in our previous studies,[41,42] the potential along the horizontal direction has a single Fourier component, whose period is the lattice length of the surface. In this paper we will consider the effect of adding a higher (second) -order Fourier component on the scattering of the particle. We find that the second-order term can lead to asymmetric scattering, to a multipeaked angular distribution and to shifts in the peak of the distribution. It makes a real difference if the second-order term is a sine or a cosine function. The former leads to asymmetric scattering while the latter leaves the scattering symmetric. When the second-order sine term is added to the first-order term one finds a ratchet like corrugation which is the source of asymmetry. When the second-order term is a cosine term, the potential remains symmetric however the second-order term may add a rich structure to the angular distribution.

In this paper we limit ourselves to in-plane scattering, so we need to consider only two degrees of freedom; the motion vertical to the surface and the horizontal motion along the surface. In Sec. II we consider the angular distribution induced by the second-order term in the absence of interaction with the surface phonons. The theory in the presence of inelastic interactions is considered in Sec. III. An analytic theory based on a Morse potential for the vertical interaction of the atom with the surface and Ohmic friction is presented in detail in Sec. IV. It is then applied to experimental data. We end with a Discussion of further implications of this study in Sec. V.

II. ELASTIC SCATTERING

A. Preliminaries

The interaction potential $V(x,z)$ (with x and z being the horizontal and vertical coordinates, respectively) has typically two components. A potential of interaction in the vertical direction $\bar{V}(z)$ and a corrugation potential. The instantaneous vertical interaction is modulated by the corrugation function $h(x)$ so that the potential of interaction is $\bar{V}(z+h(x)) \simeq \bar{V}(z)+\bar{V}'(z)h(x)$. We will therefore study the classical scattering for a particle with mass M on a surface with lattice length l whose motion is governed either by the potential

$$V_{ss}(z,x) = \bar{V}(z) + \bar{V}'(z)\left[h_1 \sin\left(\frac{2\pi x}{l}\right) + h_2 \sin\left(\frac{4\pi x}{l}\right)\right] \tag{2.1}$$

or by the potential $V_{cc}(x,y)$ where the first- and second-order corrugation terms are cosine functions, or by the potentials $V_{cs}(x,y)$ and $V_{sc}(x,y)$, where one of the two terms is a sine function and the other is a cosine function. h_1 and h_2 are, respectively, the corrugation heights for the first- and second-order terms. It is a matter of simple algebra to show the following symmetries:

$$V_{cc}\left(z,\frac{l}{2}-x\right) = V_{cc}\left(z,\frac{l}{2}+x\right), \tag{2.2}$$

$$V_{sc}\left(z,\frac{l}{4}-x\right) = V_{sc}\left(z,\frac{l}{4}+x\right), \tag{2.3}$$

$$V_{ss}\left(z,\frac{l}{2}-x\right) = -V_{ss}\left(z,\frac{l}{2}+x\right), \tag{2.4}$$

$$V_{cs}\left(z,\frac{l}{4}-x\right) = -V_{cs}\left(z,\frac{l}{4}+x\right) \tag{2.5}$$

so that the corrugation potential is symmetric for V_{cc} and V_{sc}, while it is antisymmetric for V_{ss} and V_{cs}. As we shall see below, these symmetry properties imply that the angular distribution is symmetric about the specular angle for V_{cc} and V_{sc} but it is not symmetric when the potential is a ratchet potential. Furthermore one readily finds that within each symmetry the two potentials are related to each other by a shift and reflection:

$$V_{sc}\left(z,x-\frac{1}{4}\right) = -V_{cc}(z,x), \tag{2.6}$$

and

$$V_{cs}\left(z,\frac{l}{4}-x\right) = V_{ss}(z,x). \tag{2.7}$$

In the absence of friction the classical motion is defined via the classical Hamiltonian

$$H = \frac{p_x^2+p_z^2}{2M} + V(z,x). \tag{2.8}$$

The incident particle at the time $-t_0$ is assumed to be sufficiently far from the surface and has the incident momenta p_{x0} and p_{z0}. After the collision, at the time t_0 (which is assumed to be sufficiently long such that the particle is far from the surface and no longer feels the interaction potential), the particle will have the final momenta $p_x(t_0)$, $p_z(t_0)$. The incident scattering angle is by definition

$$\theta_0 = \tan^{-1}\left(\frac{p_{x0}}{p_{z0}}\right),$$

and the scattered angular distribution is[41,42]

$$P(\theta_f) = \frac{1}{l}\int_0^l dx\,\delta\left[\theta_f - \tan^{-1}\left(\frac{p_x(t_0)}{p_z(t_0)}\right)\right]. \tag{2.9}$$

This will be our working expression below for obtaining the angular distribution.

B. Momentum shifts

To obtain the angular distribution one must estimate the final momenta after the scattering process. This is achieved by perturbation theory for which the small parameters are the corrugation heights. From Hamilton's equations for the horizontal motion and the V_{ss} potential we find that

$$p_x(t_0) = p_x(-t_0) + \delta p_x = p_x(-t_0) - \frac{2\pi}{l}\int_{-t_0}^{t_0} dt \bar{V}'(z_t) \times \left[h_1 \cos\left(\frac{2\pi x_t}{l}\right) + 2h_2 \cos\left(\frac{4\pi x_t}{l}\right)\right]. \quad (2.10)$$

The unperturbed motion in the vertical direction is such that the trajectory is at the turning point at the time $t=0$. In the horizontal direction the motion is to zeroth order that of a free particle (parallel momentum conservation), that is,

$$x_t = x(-t_0) + \frac{p_{x0}}{M}(t+t_0) \equiv x(0) + \frac{p_{x0}}{M}t. \quad (2.11)$$

Explicitly though, we do not assume parallel momentum conservation, it changes as a result of the scattering process, as determined by Eq. (2.10). Using the symmetry of the motion along the vertical direction [$\bar{V}'(z_t)$ is symmetric with respect to the time] we thus find that

$$p_x(t_0) \simeq p_{x0} - p_{z0}\left[K_1 \cos\left(\frac{2\pi}{l}x(0)\right) + K_2 \cos\left(\frac{4\pi}{l}x(0)\right)\right]. \quad (2.12)$$

where we used the notations

$$K_1 = \frac{2\pi}{l p_{z0}} h_1 \int_{-t_0}^{t_0} dt \bar{V}'(z_t)\cos(\omega_x t), \quad (2.13)$$

$$K_2 = \frac{4\pi}{l p_{z0}} h_2 \int_{-t_0}^{t_0} dt \bar{V}'(z_t)\cos(2\omega_x t), \quad (2.14)$$

and the horizontal frequency is defined as

$$\omega_x = \frac{2\pi}{l}\frac{p_{x0}}{M}. \quad (2.15)$$

In Sec. IV we show that the rainbow angle function K_1 reduces to the known result for rainbow scattering from a hard wall.[39]

The final momentum in the vertical direction is also shifted,

$$p_z(t_0) = -p_{z0} + \delta p_z = -p_{z0} + \frac{p_{x0}}{p_{z0}}\delta p_x, \quad (2.16)$$

where the second equality is derived from energy conservation.

C. Angular distribution and the sine potentials

Inserting these results into the expression for the angular distribution (2.9) and expanding to lowest order in the horizontal momentum shift, we find the interim result,

$$P_{ss}(\theta_f) = \frac{1}{l}\int_0^l dx \delta\left[\theta_f + \theta_0 - K_1 \cos\left(\frac{2\pi}{l}x\right) - K_2 \cos\left(\frac{4\pi}{l}x\right)\right], \quad (2.17)$$

where the subscript reminds us that this is the result when the corrugation potential is a sum of two sine terms. The argument of the "delta" function is nothing but the well-known deflection function of classical scattering theory as it gives the dependence of the scattering angle on the impact parameter, which is the horizontal coordinate. The integration over the delta functions is readily carried out [change variables from x to $z=K_1\cos(\frac{2\pi}{l}x)$] to find that the angular distribution is given by the expression

$$P_{ss}(\theta_f) = \frac{1}{\pi}\frac{H(K_1^2 - z_+^2)}{\sqrt{K_1^2 - z_+^2}}\left|1 - \frac{4K_2 z_+}{K_1^2}\right|^{-1} + \frac{1}{\pi}\frac{H(K_1^2 - z_-^2)}{\sqrt{K_1^2 - z_-^2}}\left|1 - \frac{4K_2 z_-}{K_1^2}\right|^{-1}, \quad (2.18)$$

where $H(x)$ is the Heaviside function and $z_\pm$ are the solutions of the quadratic equation

$$\theta_f + \theta_0 + K_2 + z - 2K_2\frac{z^2}{K_1^2} = 0, \quad (2.19)$$

so that

$$z_\pm = \frac{K_1^2 \pm K_1[K_1^2 + 8K_2(\theta_f + \theta_0 + K_2)]^{1/2}}{4K_2}. \quad (2.20)$$

As shown below, these results imply that depending on the magnitude of K_1 and K_2 one has either two or three rainbow angles, and these are no longer symmetrically distributed about the specular angle.

In the limit that the second-order corrugation is much smaller than the first-order corrugation, that is $\frac{K_2}{K_1} \ll 1$, one finds that $z_- \simeq -(\theta_f + \theta_0 + K_2)$ while $z_+ \sim K_1^2/K_2 \gg K_1$ so that it does not contribute to the angular distribution. In this limit the angular distribution reduces to

$$P_{ss}(\theta_f) = \frac{1}{\pi}\frac{H[K_1^2 - (\theta_f + \theta_0 + K_2)^2]}{\sqrt{K_1^2 - (\theta_f + \theta_0 + K_2)^2}}. \quad (2.21)$$

In the opposite limit that the first-order term vanishes ($K_1 = 0$) and only the second-order term remains, then one obtains the same result, except that K_1 must be replaced by K_2 in Eq. (2.21).

If the second-order term is weak, it causes a shift in the center of the distribution relative to the specular angle. The sign of K_2 depends on the dynamics and the incident scattering angle. The higher-order corrugation can thus induce both subspecular and superspecular scattering. We then note the asymmetry. When $z_- = K_1$ the divergence strength is $(1 - \frac{4K_2}{K_1})^{-1}$, while when $z_- = -K_1$ the divergence strength is $(1 + \frac{4K_2}{K_1})^{-1}$.

To provide further insight into the asymmetric effects that one may obtain, we plot in Fig. 1 the angular distribution

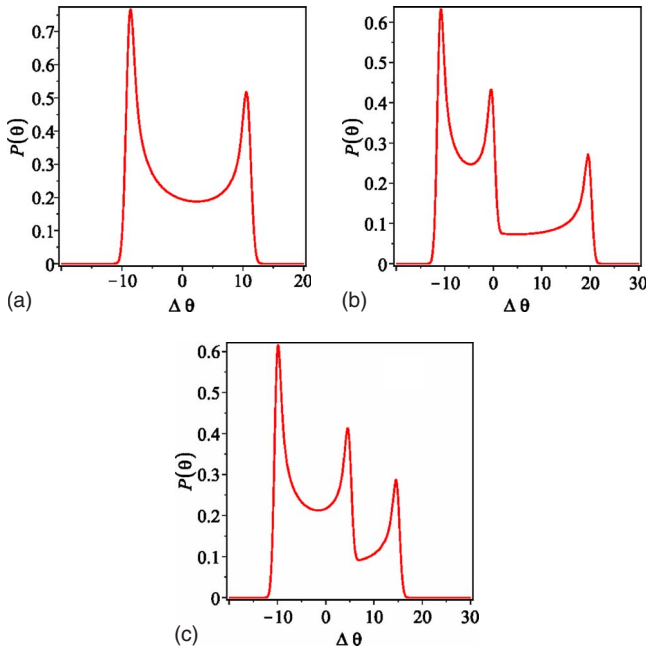

FIG. 1. (Color online) Asymmetric angular distributions—Using the sine-sine potential one obtains the angular distributions (normalized to 2π) shown in panels a–c. Panel a corresponds to a weak second-order term ($K_1=10°$, $K_2=1°$), panel b to a moderate second-order term ($K_1=K_2=10°$), and panel c to a strong second-order term ($K_1=5°$, $K_2=10°$). For further details see the text.

obtained for various values of the second-order corrugation. The angular distributions are obtained by approximating the Dirac delta function in Eq. (2.17) by a Gaussian with a small width $\gamma=0.0002$ radians^2. $\Delta\theta$ is the angular difference $\theta+\theta_{i0}$. Panel a shows the distribution with a weak second-order corrugation ($K_1=10°$, $K_2=1°$). Even a small second-order term, causes the distribution to be noticeably asymmetric. The minimum is at a superspecular angle and the two rainbows have noticeably different probabilities. Panel b of the same figure shows the angular distribution when the two rainbow angles are the same ($K_1=K_2=10°$). Now, the third peak comes into play, while the distribution remains highly asymmetric. Finally in panel c we plot a case for which the second-order term is larger than the first-order term ($K_1=5°$, $K_2=10°$).

In the examples shown in Fig. 1, the peak at superspecular angles is typically smaller than the peak at subspecular angles. This is a result of the fact that both rainbow functions K_1 and K_2 were chosen to be positive. If one of them is negative, then one obtains the opposite result, which is the subspecular peak is smaller than the superspecular peak. The sign of the rainbow functions is determined by the sign of the corrugation parameters h_1 and h_2, either of which can be positive or negative.

It is well known that the rainbow angles are defined by the points at which the derivative of the deflection function with respect to the impact parameter vanishes. As is clearly evident from Eq. (2.17) the deflection function is

$$\theta_f(x) = K_1 \cos\left(\frac{2\pi}{l}x\right) + K_2 \cos\left(\frac{4\pi}{l}x\right) - \theta_0. \quad (2.22)$$

The derivative of this function is then

$$\frac{d\theta_f(x)}{dx} = -\frac{2\pi}{l}\sin\left(\frac{2\pi x}{l}\right)\left[K_1 + 4K_2\cos\left(\frac{2\pi}{l}x\right)\right]. \quad (2.23)$$

It vanishes for $x^*=0$, $l/2$ at which $\theta_f(x^*)+\theta_0=\pm K_1+K_2$. A further rainbow angle may be found if the second term on the right-hand side of the equation vanishes. This can occur only if $|4K_2|>|K_1|$. When the second-order term is small, it introduces only an asymmetry, and there are only two rainbow angles. When it increases beyond $|K_1/4|$ one finds an additional rainbow angle at $\theta_f(x^*)=-K_2-\frac{K_1^2}{8K_2}-\theta_0$. Inspection of Fig. 1 shows that these are precisely the values of the rainbow angles.

D. Angular distribution and the cosine potentials

In this case, the momentum shift in the horizontal direction becomes

$$p_x(t_0) \simeq p_{x0} + p_{z0}\left[K_1 \sin\left(\frac{2\pi}{l}x(0)\right) + K_2 \sin\left(\frac{4\pi}{l}x(0)\right)\right], \quad (2.24)$$

and K_1 and K_2 are given as in Eqs. (2.13) and (2.14). As in the previous section we then have that the angular distribution is

$$P_{cc}(\theta_f) = \frac{1}{l}\int_0^l dx\,\delta\left[\theta_f + \theta_0 + K_1 \sin\left(\frac{2\pi}{l}x\right) + K_2 \sin\left(\frac{4\pi}{l}x\right)\right]$$

$$= \sum_{j=1}^{4} \frac{1}{2\pi K_1}\frac{1}{\left|\sqrt{1-(z_j^2/K_1^2)} - 2\kappa[1-(2z_j^2/K_1^2)]\right|}, \quad (2.25)$$

with $\kappa=K_2/K_1$ and the integration was carried out with the change in variables as before. Now one obtains a quartic equation for the variable z_j,

$$\theta_f + \theta_0 - z_j + 2\kappa z_j\sqrt{1-\frac{z_j^2}{K_1^2}} = 0, \quad (2.26)$$

where solutions in the range $-K_1 \le z_j \le K_1$ are admissible. Since $\frac{\partial z_j}{\partial \theta_f} \neq 0$ one readily finds that an extremum of the distribution is at $\theta_f=-\theta_0$, which is at the specular angle. One then finds that $P_{cc}(\theta_f+\theta_0)=P_{cc}(-\theta_f-\theta_0)$, which implies that the angular distribution is symmetric about the specular angle. This is due to the fact that the solutions of Eq. (2.26) come in pairs. If z_j^* is a solution for $\theta_f+\theta_0=\alpha$ then $-z_j^*$ is a solution when $\theta_f+\theta_0=-\alpha$. This implies, for example, that to lowest order in the small parameter κ one finds

$$P(\theta_f) = \frac{1}{\pi\sqrt{K_1^2-(\theta_f+\theta_0)^2}} + O(\kappa^2). \quad (2.27)$$

One can work through the analysis for the deflection function in this case too. However, the rainbow angles are now given as solutions of a quadratic equation, so the analysis is somewhat more complex.

Here too we provide some plots which demonstrate the effect of the second-order term. Panel a of Fig. 2 shows the

angular distribution [obtained as in the asymmetric case by approximating the Dirac delta function in Eq. (2.17) by a Gaussian with a small width $\gamma=0.0002$ radians^2] with a weak second-order corrugation ($K_1=10°$, $K_2=1°$). In this case, the small second-order term is hardly felt, the distribution remains double peaked and symmetric about the specular angle. Increasing the second-order contribution such that $K_1=K_2=10°$ leads to a four peaked distribution, one now "sees" the four rainbow angles. Finally in panel c we plot a case for which the second-order term is larger than the first-order term ($K_1=5°$, $K_2=10°$).

It remains to consider the cases of $P_{cs}(\theta_f)$ and $P_{sc}(\theta_f)$. As already shown in Eq. (2.7) the potential V_{cs} is a ratchet potential, which can be transformed into the potential V_{ss} so it has the same angular distribution. Similarly the angular distribution for the potential V_{sc} is the same as the angular distribution for the potential V_{cc}.

III. INELASTIC SCATTERING

A. Model Hamiltonian

We assume that both the vertical and horizontal coordinates fluctuate due to interaction with the thermal phonon bath of the surface. We then use the same framework as in Ref. 42. The interaction of the horizontal motion with the phonon bath is modeled with a coupling between the horizontal coordinate and the bath, which is linear in the bath coordinates and modulated by a space-dependent function $g(z)$, which vanishes when the vertical coordinate is large. In the presence of the phonon bath, the vertical coordinate fluctuates so that the interaction potential of the incident atom with the surface would be $\bar{V}(z-\delta z)$. Allowing only small fluctuations

$$\bar{V}(z-\delta z) \simeq \bar{V}(z) - \delta z \frac{d\bar{V}(z)}{dz} \tag{3.1}$$

leads us to assuming that the Hamiltonian governing the scattering event is

$$\begin{aligned} H = {} & \frac{p_x^2+p_z^2}{2M} + V_{mn}(z,x) \\ & + \frac{1}{2}\sum_{j=1}^{N}\left\{ p_{j_z}^2 + \omega_{j_z}^2\left[x_{j_z} - \frac{c_{j_z}\sqrt{M}}{\omega_{j_z}^2}\bar{V}'(z)\right]^2\right\} \\ & + \frac{1}{2}\sum_{j=1}^{N}\left\{ p_{j_x}^2 + \omega_{j_x}^2\left[x_{j_x} - \frac{c_{j_x}\sqrt{M}}{\omega_{j_x}^2}\frac{l}{2\pi}\sin\left(\frac{2\pi x}{l}\right)g(z)\right]^2\right\}, \\ & m=s,c;\quad n=s,c. \end{aligned} \tag{3.2}$$

The horizontal and vertical bath degrees of freedom are characterized by the mass weighted momenta and coordinates p_{j_i}, x_{j_i}, $j=1,\ldots,N$; $i=x,z$. Translational invariance of the model is assured since the term coupling the horizontal motion to the respective phonon bath is periodic in the horizontal coordinate. When the particle is far from the surface it does not interact with the phonons, so that the bath Hamiltonian (in mass weighted coordinates and momenta) is defined to be

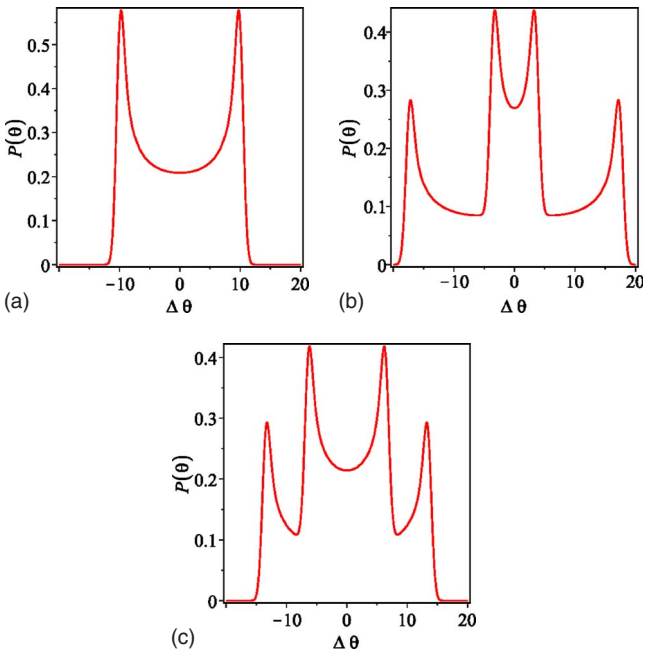

FIG. 2. (Color online) Symmetric angular distributions—Using the cosine cosine potential one obtains the angular distributions (normalized to 2π) shown in panels a–c. Panel a corresponds to a weak second-order term ($K_1=10°$, $K_2=1°$), panel b to a moderate second-order term ($K_1=K_2=10°$), and panel c to a strong second-order term ($K_1=5°$, $K_2=10°$). For further details see the text.

$$H_B = \frac{1}{2}\sum_{j=1,\ i=x,z}^{N}(p_{j_i}^2 + \omega_{j_i}^2 x_{j_i}^2). \tag{3.3}$$

As is well known, for the linearly coupled harmonic baths the equations of motion in the continuum limit are generalized Langevin equations (GLEs). Introducing the spectral densities

$$J_i(\omega) = \frac{\pi}{2}\sum_{j=1}^{N}\frac{c_{j_i}^2}{\omega_{j_i}}\delta(\omega-\omega_{j_i}), \quad i=x,z \tag{3.4}$$

and associated friction functions

$$\eta_i(t) = \frac{2}{\pi}\int_0^\infty d\omega \frac{J_i(\omega)}{\omega}\cos(\omega t), \quad i=x,z, \tag{3.5}$$

the GLE for the horizontal motion takes the form (as may be readily seen by using the known forced harmonic oscillator solution for the bath variables and inserting it into the equations of motion for the system degrees of freedom)

$$\begin{aligned} & \sqrt{M}F_x(t)\cos\left(\frac{2\pi x_t}{l}\right)g(z_t) \\ & = M\ddot{x}_t + \frac{\partial V(z_t,x_t)}{\partial x_t} + M\cos\left(\frac{2\pi x_t}{l}\right)g(z_t) \\ & \quad \times \int_{-t_0}^{t} dt'\,\eta_x(t-t')\left\{\frac{d}{dt'}\left[\frac{l}{2\pi}\sin\left(\frac{2\pi x_{t'}}{l}\right)g(z_{t'})\right]\right\}. \end{aligned} \tag{3.6}$$

The GLE for the vertical motion is more complicated, but is not needed explicitly. As in the previous section for the pure system dynamics, the unperturbed vertical motion is taken to be an even function of time, such that the particle reaches the vertical turning point at time $t=0$. Trajectories are initiated at the time $-t_0$. The projectile is initially sufficiently distant from the surface, such that at the vicinity of z_0 all the coupling functions vanish and the motion is that of a free particle. The noise functions

$$F_i(t) = \sum_{j=1}^{N} c_{j_i}\left(x_{j_i} \cos[\omega_{j_i}(t+t_0)] + \frac{p_{j_i}}{\omega_{j_i}} \sin[\omega_{j_i}(t+t_0)] \right),$$

$$i = x,z \tag{3.7}$$

therefore depend only on the initial conditions of the respective phonon bath. They obey the fluctuation dissipation relations

$$\langle F_i(t_1)F_j(t_2)\rangle = \delta_{ij}\frac{M}{\beta}\eta_i(t_1-t_2), \quad i,j=x,z, \tag{3.8}$$

where $\beta=1/k_BT$ is the inverse temperature (k_B is Boltzmann's constant) and the averaging is over the thermal distribution associated with the classical bath Hamiltonian as given in Eq. (3.3).

B. Classical perturbation theory

1. Energy loss and the change in the final momenta

When considering the motion of a rare gas projectile whose interaction with the surface and the phonons does not include any strong chemical interactions, it is reasonable to assume that the system bath couplings are weak and Ohmic,

$$\eta_i(t) = 2\eta_i\delta(t), \quad i=x,z. \tag{3.9}$$

As in our previous work and in the previous section, we will follow a perturbation approach toward deriving the angular distribution. Explicit expressions for the final momenta, the averaged, and fluctuational energy losses of the incident particle to the bath are provided in Appendix A. Here, we note that for the "ss" potential of Eq. (2.1), to first order in the corrugation heights, friction coefficients, and noise strengths, we find (see also Ref. 42) from the GLE [Eq. (3.6)] that the final momentum in the horizontal direction is given by the expression

$$\begin{aligned} p_x(t_0) &\simeq p_{x0} - p_{z0}\left[K_1 \cos\left(\frac{2\pi}{l}x(0)\right) + K_2 \cos\left(\frac{4\pi}{l}x(0)\right)\right] \\ &\quad + \Delta p_{x,1} + \Delta p_{x,2} \\ &\equiv p_{x0} + \delta p_{x0}. \end{aligned} \tag{3.10}$$

Comparing to the previous result in the absence of friction 2.12, we note that the coupling to the phonon bath induces a frictional momentum shift $\Delta p_{x,1}$ and a noise induced momentum shift $\Delta p_{x,2}$. Explicit expressions are given in Appendix A.

The energy loss to the bath (see Refs. 48 and 42) may be divided into two parts, an average energy loss, and a fluctuational energy loss,

$$\Delta E_B = \sum_{i=x,z} (\langle \Delta E_B\rangle_i + \delta E_{B_i}). \tag{3.11}$$

These have been further subdivided into separate average and fluctuational energy losses in the horizontal and vertical directions. Explicit expressions for the energy losses are given in Appendix A, here we note that the energy losses depend on the initial impact parameter.

The variances of the fluctuational energy losses are proportional to the average energy losses,

$$\langle \delta E_{B_i}^2\rangle = \frac{2}{\beta}\langle \Delta E_B\rangle_i, \quad i=x,z. \tag{3.12}$$

The shift in the final momentum in the vertical direction is obtained via energy conservation as in the uncoupled case, except that here one has to take into consideration the energy losses to the phonon baths,

$$p_z\delta p_z = M\Delta E_B + p_x\delta p_x. \tag{3.13}$$

2. Angular distribution

The expression for the angular distribution has the same form as in the uncoupled case, except that now one has to include the averaging over the phonon baths. For this purpose we note

$$\tan^{-1}\left(\frac{p_x(t_0)}{p_z(t_0)}\right) \simeq -\theta_{i0} + \delta\theta_i, \tag{3.14}$$

where to lowest order in the momentum shifts

$$\delta\theta_i \equiv -\frac{\delta p_x}{p_{z0}} - \frac{\cos^2(\theta_{i0})}{p_{z0}^2}\frac{p_{x0}}{p_{z0}}M\Delta E_B. \tag{3.15}$$

The integration over the bath variables is effected as in Appendix A of Ref. 42. One finds that the angular distribution is given by the expression

$$P(\theta) = \frac{1}{l}\int_0^l dx(t_0)\frac{1}{\sqrt{\pi\Sigma^2(x(t_0))}}\exp\left(-\frac{\left(\theta+\theta_{i0}-K_1(p_{x0},p_{z0})\cos\left(\frac{2\pi}{l}x(t_0)\right)-K_2(p_{x0},p_{z0})\cos\left(\frac{4\pi}{l}x(t_0)\right)+\Delta\theta_1(x(t_0))\right)^2}{\Sigma^2(x(t_0))}\right), \tag{3.16}$$

where the variance is

$$\Sigma^2[x(t_0)] = \frac{\tan^2(\theta_{i0})}{\beta E_0}\left(\frac{\langle \Delta E_B\rangle}{E_0} + \eta_x \int_{-t_0}^{t_0} dt g^2(z_t)\left\{1 - 2\cos\left[\frac{4\pi}{l}x(t_0)\right]\right\}\right) + \frac{\eta_x}{\beta E_0}\left(\int_{-t_0}^{t_0} dt g^2(z_t)\left\{1 + \frac{\cos\left[\frac{4\pi}{l}x(t_0)\right]\cos(2\omega_x t)}{\cos^2(\theta_{i0})}\right\}\right) \tag{3.17}$$

and the angular shift is

$$\Delta\theta_1(x(t_0)) = \tan(\theta_{i0})\left(\frac{\langle \Delta E_B\rangle}{2E_0} - \frac{\eta_x}{2}\int_{-t_0}^{t_0} dt g^2(z_t)\right). \tag{3.18}$$

These expressions are identical in form to the previous expressions derived for in plane scattering in Ref. 42. The important difference comes from the added term in the corrugation. This induces the extra structure in the angular distribution, as already described qualitatively in the previous section. The coupling to the phonon bath smoothens the distribution. If the coupling is strong, the phonon coupling will dominate and the distribution will be a single bell-shaped Gaussian-like peak. However for weak coupling one will observe a Gaussian like broadening of the multiple peaks and the asymmetric structures described in the previous section.

IV. EXAMPLES AND EXPERIMENTAL APPLICATIONS

A. Analytical results for a Morse oscillator model

The theory developed in the previous section can be solved to a certain extent analytically if one chooses the vertical potential to be the Morse oscillator potential,

$$\bar{V}(z) = V_0[1 - \exp(-\alpha z)]^2 - V_0. \tag{4.1}$$

The trajectory for the vertical motion is known analytically,

$$\exp(\alpha z_t) = -\frac{\cos(\Phi)}{\sin^2(\Phi)}[\cosh(\Omega t) + \cos(\Phi)], \tag{4.2}$$

where the frequency Ω is:

$$\Omega^2 = \frac{2\alpha^2 E_z}{M} = \frac{\alpha^2 p_{z0}^2}{M^2}, \tag{4.3}$$

and we used the notation

$$\cos(\Phi) = -\sqrt{\frac{V_0}{(E_z + V_0)}}, \quad \sin(\Phi) = \sqrt{\frac{E_z}{(E_z + V_0)}}. \tag{4.4}$$

Explicit expressions for the rainbow angle functions can be obtained by noting that

$$I_1 = \frac{1}{\Omega}\int_0^\infty d\tau \cos(\bar{\Omega}\tau)[\cosh(\tau) + \cos(\Phi)]^{-1} = \frac{\pi \sinh(\bar{\Omega}\Phi)}{\Omega \sin(\Phi)\sinh(\bar{\Omega}\pi)}. \tag{4.5}$$

Using the notation

$$I_n = \frac{1}{\Omega}\int_0^\infty d\tau \cos(\bar{\Omega}\tau)[\cosh(\tau) + \cos(\Phi)]^{-n}, \tag{4.6}$$

one has the recursion relation

$$I_{n+1} = \frac{1}{n \sin(\Phi)}\frac{\partial I_n}{\partial \Phi}. \tag{4.7}$$

One then finds that the analytical expressions for the rainbow angle functions are

$$K_1(p_0, \theta_{i0}) = \frac{4\pi^2 h_1 \bar{\Omega}\cosh(\bar{\Omega}\Phi)}{l \sinh(\bar{\Omega}\pi)}, \tag{4.8}$$

$$K_2(p_0, \theta_{i0}) = \frac{16\pi^2 h_2 \bar{\Omega}\cosh(2\bar{\Omega}\Phi)}{l \sinh(2\bar{\Omega}\pi)}, \tag{4.9}$$

with

$$\bar{\Omega} = \frac{\omega_x}{\Omega} = \frac{2\pi}{\alpha l}|\tan(\theta_{i0})|. \tag{4.10}$$

Through the argument of the "delta" function in Eq. (2.17) this then gives an analytical expression for the deflection function.

One may readily relate these expressions with the "classical" expression for rainbow scattering[39] when the potential in the vertical direction is a hard wall by taking the limit that the Morse stiffness parameter $\alpha \to \infty$. One finds for example, that

$$\lim_{\alpha\to\infty} K_1(p_0, \theta_{i0}) = \frac{4\pi h_1}{l}, \tag{4.11}$$

and this is the weak corrugation limit of the known expression for hard wall rainbow scattering

$$\frac{\theta_{rainbow} + \theta_{i0}}{2} = \pm \tan^{-1}\left(\frac{2\pi h_1}{l}\right). \tag{4.12}$$

The angle Φ goes from π to $\pi/2$ as the vertical energy increases from 0 to ∞. This implies that the rainbow angle functions decrease as the energy increases. More interest-

ingly, the ratio of the second-order rainbow function to the first-order rainbow function

$$\frac{K_2(p_0,\theta_{i0})}{K_1(p_0,\theta_{i0})} = \frac{2h_2\cosh(2\bar{\Omega}\Phi)}{\cosh(\bar{\Omega}\pi)h_1\cosh(\bar{\Omega}\Phi)} \tag{4.13}$$

also decreases as a function of energy. This means that typically the asymmetry induced by the second-order term will be smaller as the energy increases.

To complete the theory it is necessary to specify the function $g(z)$ which couples the phonons to the horizontal motion. We choose the function $g(z)$ which scales the lateral corrugation in Eq. (3.2) to be consistent with the attenuation of the repulsive component of the Morse potential (4.1):

$$g(z) = \exp(-2\alpha z). \tag{4.14}$$

The resulting expressions for the various energy losses and shifts are given in Appendix B. One can then compute the angular distribution with a single remaining numerical integration over the horizontal coordinate.

Within this Morse oscillator model we have six free parameters—the well depth of the Morse oscillator V_0; the Morse oscillator stiffness parameter α; the corrugation parameters h_1 and h_2; and the Ohmic friction coefficients η_x and η_z. The lattice length l and the mass M are assumed to be known. In the following subsections we will use this model to analyze experimental results for the scattering of atoms on surfaces.

B. Experimental applications

1. Preliminaries

In this subsection we will apply the theory to a number of experimental examples in which the underlying potential is symmetric while the measured angular distribution is asymmetric. This calls into question our whole approach. For example, for scattering of Ar on LiF(100) it is evident that the potential energy surface is symmetric. It would then be seemingly unjustified to use an asymmetric fitting of the surface. However as noted by Tully[38] when considering the washboard model, "the probability $P_2(x)$ of striking the surface at position x is not uniform. There is a larger probability of striking a region where the surface slopes toward the incoming beam than where the surface slopes away." If the corrugation function is $h(x)$ then the probability is[38]

$$P_2(x) = \frac{1}{l}\left[1 - \frac{dh(x)}{dx}\tan(\theta_{i0})\right]. \tag{4.15}$$

Consider then the simple sinusoidal corrugation function

$$h(x) = h\sin\left(\frac{2\pi x}{l}\right).$$

The effective corrugation $h_{eff}(x)$ "seen" by the incident particle is then a product of the probability of arriving at the point x and the actual corrugation at that point,

$$\begin{aligned} h_{eff}(x) &= P_2(x)h(x) \\ &= \frac{h}{l}\left[1 - \frac{2\pi h}{l}\cos\left(\frac{2\pi x}{l}\right)\tan(\theta_{i0})\right]\sin\left(\frac{2\pi x}{l}\right) \\ &= \frac{h}{l}\sin\left(\frac{2\pi x}{l}\right) - \frac{\pi h^2}{l^2}\tan(\theta_{i0})\sin\left(\frac{4\pi x}{l}\right), \end{aligned} \tag{4.16}$$

showing explicitly how the asymmetry created by the actual path of the particle may be modeled in terms of an added higher-order sin term in the corrugation.

Within the perturbation theory approach used in this paper, this asymmetry does not arise when using a single term for the corrugation. One notes that the second-order term goes as h^2 while the perturbation theory is correct only to order h. From a physical point of view one derives the asymmetry within the washboard model by noticing that for different values of the impact parameter, the particle encounters the hard wall at different vertical positions. In other words, the vertical potential encountered by the particle depends on the impact parameter. Within the first-order perturbation theory, the vertical potential felt by the particle is independent of the impact parameter, hence the asymmetry does not appear naturally within it. However, it may be modeled by adding in the second-order sin term. This then creates an effective deflection function which is asymmetric and leads to asymmetry in the angular distribution. This is the procedure we employ in this paper to fit the experimental results.

2. Scattering of Ar on LiF(100)

Kondo *et al.*[28] recently reported their finding for the experimental angular distributions of Ar atoms scattered from a LiF(001) surface (in the [100] direction) as a function of incident energy at a fixed 45° angle of incidence. Their experimental setup is such that the width of the incident beam is typically 1 degree or less, thus providing very well-characterized angular distributions. At all measured energies they find an asymmetric double peaked angular distribution, typical of rainbow scattering. They find that the rainbow angles decrease with increasing incident energy. They fit their experimental results to the washboard model, albeit by using a different rainbow angle for each energy separately. Their rainbow angle parameter decreases with increasing energy from a value of 10.4° at 315 meV to 7.0° at 705 meV incident energy. They consider this to be a counterintuitive lessening of corrugation with increasing energy.

We used the Morse potential model for the same data. We use the atomic mass of Ar for the projectile ($M=39.948$), the well depth $V_0=88$ meV as reported in Ref. 49, and the lattice length $l=4$ Å as measured by Ekinci and Toennies.[50] The remaining parameters were set to $\alpha=1/2$ Å^{-1}, $h_1=-0.1217$ Å, $h_2=0.1428$ Å, and $\eta_x/\omega_0=.0002536$, where $\omega_0=\alpha\sqrt{(2V_0/M)}$ is the harmonic frequency of the Morse potential and $M^2\omega_0^3\eta_z=0.001820$. The last two friction parameters are given in reduced form and show that the friction is weak. We note that this is a five parameter theory, as all other parameters were obtained from experimental knowledge.

The results are shown in Fig. 3, where we plot the theoretical angular distributions as solid lines and the experimental angular distribution as solid circles for the incident ener-

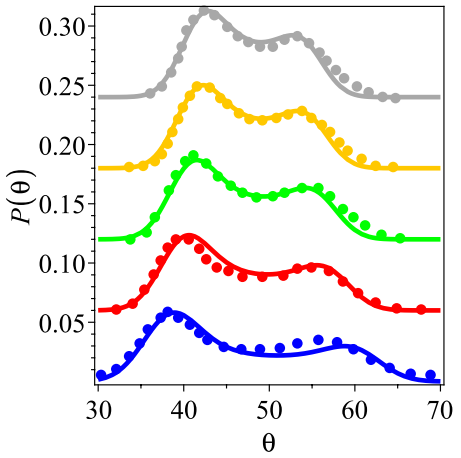

FIG. 3. (Color online) Angular distributions for the scattering of Ar on a LiF(100) surface. The solid lines show the angular distributions obtained with the Morse potential model at the incidence angle of 45 degrees. The solid circles are the experimental angular distributions from the paper by Kondo *et al.* (Ref. 28). The heights of the experimental distributions were normalized to agree with the normalized theoretical distributions. The plots from bottom to top show the angular distributions for the energies 315, 435, 525, 620, and 705 meV, respectively. Each distribution is shifted vertically from the previous one by 0.06. Note the quantitative agreement between experiment and theory.

gies of 315, 435, 525, 620, and 705 meV, respectively. The angle of incidence is 45° and the surface temperature was taken to be 300 °K. We find that the theory fits the experimental distributions quantitatively; the fits are slightly better than those reported by Kondo *et al.* using the washboard model. Perhaps most notable is the fact that we did not have to fit each distribution separately; the theory accounts correctly for the energy dependence of the rainbow angles. We also note that the distributions are not symmetric; it was necessary to add the second-order corrugation term. In Fig. 4 we plot the incident energy dependence of the rainbow angle

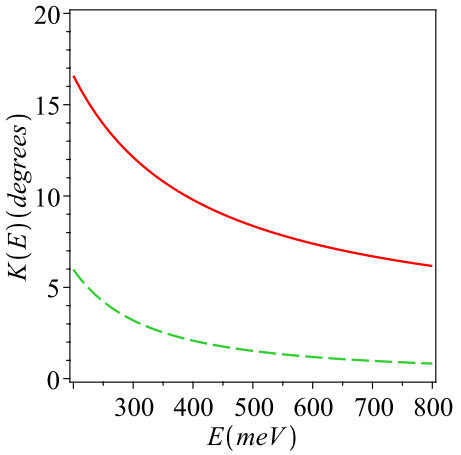

FIG. 4. (Color online) Incident energy dependence of the (absolute value of the) rainbow angle functions for the scattering of Ar on LiF(100). The solid line is for K_1 the dashed line for K_2. The model parameters are the same as for Fig. 3. Note the decrease in the rainbow angle functions with increasing incident energy.

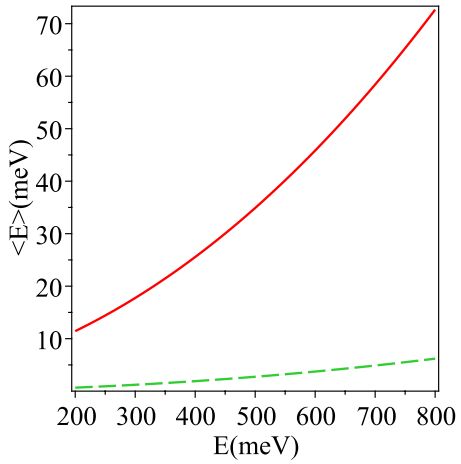

FIG. 5. (Color online) Incident energy dependence of the average energy loss in the vertical (solid line) and horizontal (dashed line) directions. The parameters are the same as used for Figs. 3 and 4. Note the increase in the average energy losses with incident energy.

functions K_1 and K_2. One notes that both functions decrease with increasing energy, even though the corrugation parameters are of course fixed.

The decrease in the rainbow angles with energy is a result of the dynamics and does not imply that the corrugation becomes smaller with increasing energy, as suggested by Kondo *et al.* In fact, as the energy increases, so does the energy loss, as shown in Fig. 5 for the same system. Here the solid line is the energy loss along the vertical direction while the dashed line is the energy loss in the horizontal direction. One notes that both energy losses increase with increasing energy, as expected intuitively. As the energy increases, the atom creates a larger displacement of the surface atoms. Interestingly, the relative average energy losses (the ratio of the energy loss to the incident energy) are a decreasing function of the energy.

3. Scattering of Xe on Ge(100)

Amirav *et al.*[31] published measured angular distributions for the scattering of Xe on the Ge(100) surface at different incidence angles and different temperatures. At the incidence energy of 2.4 eV and 45° incidence scattering angle, they find an asymmetric double peaked distribution. Increasing the scattering angle to 70° leads to a single peaked distribution. Increasing the temperature of the surface from $T=297$ °K to $T=823$ °K washes out the double peaked structure, leading to a single peak whose maximum is somewhat larger than the specular angle.

As we shall show, there is good agreement between theory and experiment. In Ref. 51 the speed ratios of the incident beam are reported as ranging between 5 and 8%. This implies that our theoretical results must take this broadening into account. To simplify, we accounted for this experimental broadening by adding a constant width of 0.2 radians to the width of the angular distribution as given in Eq. (3.17).

In panel a of Fig. 6 we plot the broadened angular distributions obtained from the Morse potential model using the

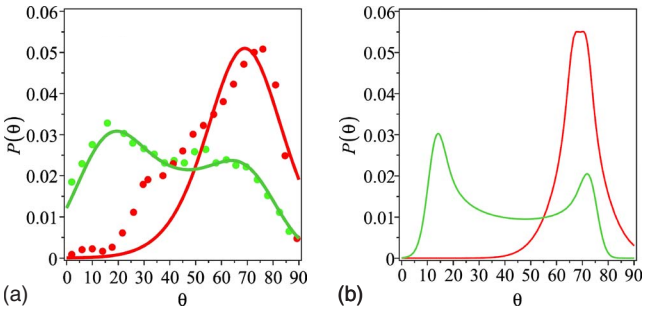

FIG. 6. (Color online) Angular distributions for the scattering of Xe on a Ge(100) surface. The solid lines in panel a show the angular distributions obtained with the Morse potential model at the incidence angles of 45 and 70 degrees. The solid circles are the experimental angular distributions at the same angles of incidence adapted from the paper by Amirav *et al.* (Ref. 31). The normalized theoretical distributions without the added empirical broadening are shown in panel b. For further details, see the text.

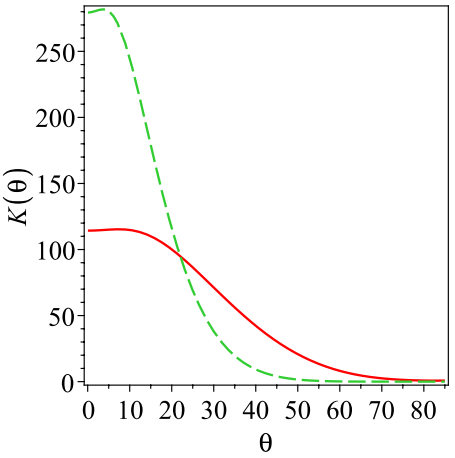

FIG. 7. (Color online) Incident angle dependence of the (absolute value of the) rainbow angle functions for the scattering of Xe on Ge(100). The solid line is for K_1 the dashed line for K_2. The model parameters are the same as for Fig. 6. Note the sharp decrease in the rainbow angle functions with increasing incident scattering angle.

parameter values $V_0=250$ meV,[52] $l=6$ Å, $\alpha=1/3$ Å^{-1}, $M=131.29$ a.m.u, $h_1=-0.952$ Å, $h_2=1.164$ Å, $\eta_x/\omega_0=0.0102$, and $M^2\omega_0^3\eta_z=0.002675$. The temperature $T=297$ °K. The solid lines correspond to the theoretical angular distributions for the incident angles of 45° and 70° while the solid circles are the experimental results, adapted from Ref. 31. The normalized theoretical angular distribution at 45° and 70° angles of incidence are multiplied, respectively, by the constant factors of 2.08 and 1.96 so as to have the same peak height as the (un-normalized) experimental distributions. Panel b shows the normalized theoretical distributions without the artificial broadening width of 0.2 radians. We note that the theory is able to account for both the asymmetry in the angular distribution at the incidence angle of 45° as well as the fact that for an incidence angle of 70° one remains with a single bell shaped function.

The disappearance of the double peaked structure at the higher incident angle is well understood by considering the angular dependence of the rainbow functions as a function of the incident scattering angle as shown in Fig. 7, using the same set of parameters as in Fig. 6. One notes that the rainbow angle functions decrease rapidly with increasing scattering angle. For $\theta_0=70°$ $K_1\simeq 2°$ so that thermal averaging induced by the phonons masks the double peaked structure. When $\theta_0=45°$ the rainbow width $K_1=20°$ is larger than the variance of the distribution induced by coupling to the phonons and so one remains with a double peaked distribution.

The analysis of the scattering of Xe on Ge complements the analysis of the scattering of Ar on LiF. For the former case, we showed that our theory naturally accounts for the disappearance of the rainbow scattering feature as the angle of incidence is increased at a fixed incident energy. For the latter, we showed that the theory accounts well for the energy dependence of the angular distribution at a fixed angle of incidence.

There is though a serious shortcoming of the theory. For the large scattering angle of 70°, the theory allows for a finite probability of scattering at angles greater than 90°, something which is physically impossible. This is a result of the first-order perturbation theory used, and it is insufficient. At grazing angles, the momentum in the vertical direction is much smaller than the momentum in the horizontal direction so that the assumption of weak coupling breaks down.

The fits are not too sensitive with respect to the parameters used. We cannot pinpoint the well depth; however the range of acceptable well depths is 200–300 meV. Likewise, the friction coefficients may be changed by 20%–30%. The ratio of the corrugation parameters is more sensitive; a good fit to the experiment would allow a variation by no more than 20%. In other words, the parameters used provide a general picture of the acceptable range, which is consistent with known properties of the system as well as with the experimental results. More detailed experimental results would provide a more stringent test of the theory. For example, measurement of the energy loss as a function of energy would pinpoint the magnitude of the friction coefficients. Here, we do note that our choice of the coupling functions between the horizontal motion and the phonon bath as given in Eq. (4.14) is qualitative. Different coupling functions could lead to different choices for the friction coefficient.

4. Scattering of Ar on Ag(100)

The experimental results presented in Ref. 31 show that the angular distribution evolves from a slightly asymmetric angular distribution at an angle of incidence of 30°, to a symmetric double peaked distribution at 45° to a single bell shaped distribution at 60°. The surface temperature is not reported in the paper, we assume that it is room temperature (297 °K). The model parameters used in this case are $V_0=70$ meV,[52] $l=2.8$ Å,[23] $\alpha=1.0714$ Å^{-1}, $M=39.948$ a.m.u, $h_1=-0.1057$, $h_2=0.0106$ Å, $\eta_x/\omega_0=0.001\,39$, and $M^2\omega_0^3\eta_z=0.000\,908$. The incident energy is 2500 meV.

As in the case of the scattering of Xe on the Ge(100) system, here too, the experimental distributions are broadened. In Fig. 8(a) we compare the theoretical results (broad-

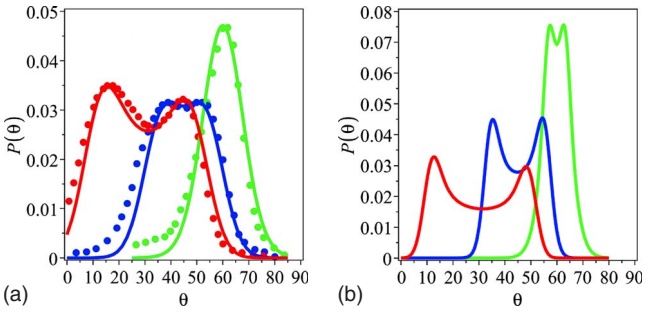

FIG. 8. (Color online) Angular distributions for the scattering of Ar on a Ag(100) surface. The solid lines in Panel a show the angular distributions obtained with the Morse potential model at the incidence angles of 30, 45, and 60 degrees. The normalized distributions were multiplied with a constant factor of 1.54, 1.02, and 0.92 for the angles of incidence of 30, 45, and 60 degrees, respectively, to facilitate the comparison. One can identify each distribution according to its center, which is roughly at the specular angle. The solid circles are the respective experimental angular distributions at the same angles of incidence adapted from the paper by Amirav *et al.* (Ref. 31). Panel b shows the corresponding normalized theoretical distributions without the added broadening. For further details, see the text.

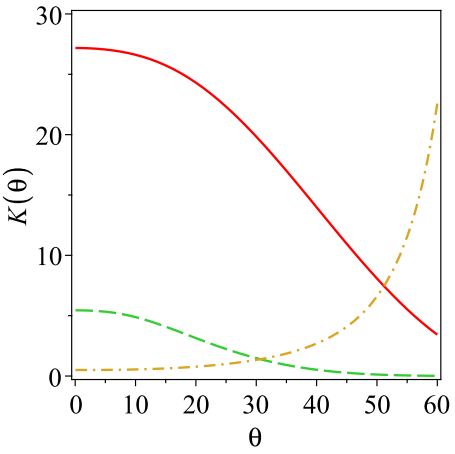

FIG. 9. (Color online) Incident angle dependence of the (absolute value of the) rainbow angle functions for the scattering of Ar on Ag(100). The solid line is for K_1 the dashed line for K_2, the dashed dotted line shows the ratio $K_1/K_2/10$. The model parameters are the same as for Fig. 8. Note the sharp decrease in the rainbow angle functions with increasing incident scattering angle and the sharp increase in the ratio of K_1/K_2 with increasing incidence angle. This sharp increase indicates that the asymmetry will disappear as the angle of incidence is increased.

ened with a fixed width of 0.085 radians) with the measured results of Amirav *et al.*[31] One notes the quantitative agreement. The asymmetry here is smaller than the asymmetry found in the Xe-Ge(100) or the Ar-LiF(100) system. However, the trend is the same. The rainbow scattering appears at low incident scattering angle and disappears as the scattering angle is increased. This is seen more clearly in panel b of Fig. 8 where we plot the normalized angular distributions without the added broadening. As may be also seen from Fig. 9, the rainbow function K_2 falls off faster with increasing angle of incidence than the function K_1. Therefore at the incidence angle of 45° one still sees the rainbow scattering however the asymmetry is almost gone. Increasing the angle of incidence to 60° wipes out the rainbows completely and one remains with a single peaked distribution.

5. Scattering of Kr on Ag(100)

This system is the most asymmetric of all systems analyzed in this paper. We have used the following parameters for this case: $V_0=100$ meV,[52] $l=2.8$ Å,[23] $\alpha=2.143$ Å^{-1}, $M=83.8$ a.m.u, $h_1=-0.0450$, $h_2=0.0476$ Å, $\eta_x/\omega_0=0.000603$, and $M^2\omega_0^3\eta_z=0.000431$. The incident energy is 6600 meV and $T=297$ K.

The resulting angular distributions broadened by a constant factor of 0.09 radians are compared in panel a of Fig. 10 with the experimental measurements. The fit in this case, is not as good as in the previous ones, especially at the 45° angle of incidence. The normalized theoretical distributions without an extra broadening are shown in panel b. One notes that the asymmetry is so strong that we predict a three peaked distribution when the incident angle is 30° and that the rainbow scattering may still be observed when the incident angle is 60°. For the parameter set used, the average energy loss in the horizontal and vertical directions is 759 and 2467 meV, respectively. We note that qualitatively the theory accounts well for the experimental observations. The distance between the two central rainbows decreases with increasing scattering angle, as does the asymmetry. This is again well understood by looking at the (absolute value of the) incidence angle dependence of the rainbow functions as plotted in Fig. 11. K_1 decreases with increasing incidence angle as does K_2, but more importantly, the ratio $|K_1/K_2|$ increases with increasing angle of incidence, explaining why the asymmetry becomes less important.

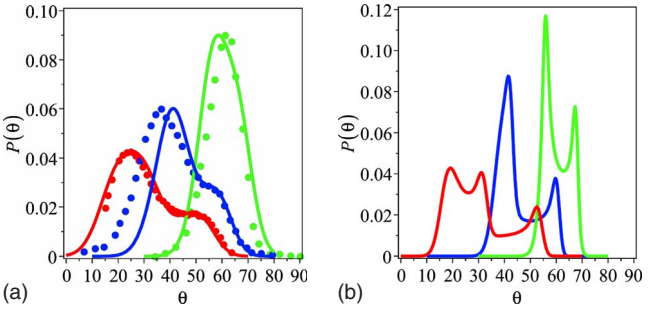

FIG. 10. (Color online) Angular distributions for the scattering of Kr on a Ag(100) surface. Panel (a) compares the angular distributions obtained with the Morse potential model (solid lines) at the incidence angles of 30, 45, and 60 degrees with the experimental results (solid circles) adapted from Ref. 31. The normalized distributions were multiplied with a constant factor of 1.3, 1.35, and 1.78 for the angles of incidence of 30, 45, and 60 degrees, respectively, to facilitate the comparison. One can identify each distribution according to its center, which is roughly at the specular angle. Panel (b) shows the normalized theoretical distributions without the added broadening used for comparison to the experimental results. Note the predicted three peaked distribution at the 30° angle of incidence. For further details, see the text.

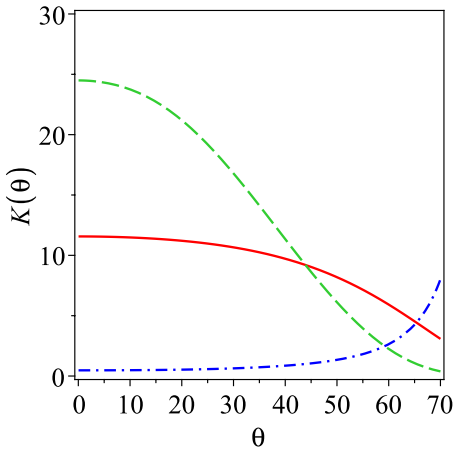

FIG. 11. (Color online) Incident angle dependence of the (absolute value of the) rainbow angle functions for the scattering of Kr on Ag(100). The notation is as in Fig. 9, the model parameters are the same as for Fig. 10.

V. DISCUSSION

The central theme of this paper is a theory of rainbow scattering for ratchet potentials. We have shown how addition of a single higher order (sine) term to the potential induces asymmetric rainbow scattering as well as additional rainbow angles. The theory includes interaction with two independent phonon baths: one associated with the vertical motion, the other with the horizontal motion. It is important to note that as in Ref. 42 the Hamiltonian we used is periodic (with respect to the lattice length) in the horizontal coordinate. As a result the angular shift $\Delta\theta_1$ is periodic in the horizontal coordinate and this can also induce a further asymmetry to the dynamics. The interesting topic of phonon induced rainbows, which emerges from this observation, will be considered separately elsewhere.[53]

Analytic formulas have been derived with a Morse oscillator model. These are especially useful for obtaining a qualitative understanding of the dependence of the rainbow angles on different features of the scattering. We have shown that both rainbow angle functions decrease with increasing angle of incidence; however the primary rainbow angle K_1 decreases less than the secondary function K_2. This leads to two important qualitative features, observed experimentally. The distance between the rainbow angles decreases with increasing scattering angle, while the asymmetry decreases.

Our theory gives excellent agreement with the experimental results of Kondo *et al.*[28] for the scattering of Ar on LiF. We also applied the theory to the measurements of Amirav *et al.*[31] and found good agreement with experiment for all three systems analyzed. All of these systems are symmetric, so that in principle the corrugation function should be symmetric. However, we noted that the asymmetry which is induced by the actual flight of the particle as it approaches the surface is well modeled in terms of the second-order sine term in the corrugation function. Thus the asymmetric corrugation function used to fit the experiment should be considered as an effective corrugation.

The Morse oscillator based theory has many parameters in it. However, a thorough experimental measurement would limit the parameter fitting. Ideally, the experiment would provide information on the energy loss as a function of incidence energy. This would provide direct input for estimating the friction parameters since they "control" the energy loss. Similarly, the asymmetry of the distribution is determined by the corrugation parameter of the second-order term in the horizontal potential, while the rainbow angles at a single energy determine the corrugation height of the first-order term. The well depth for the Morse potential can be estimated from *ab initio* structure computations. Thus the only really meaningful parameter which is more difficult to pin down is α the stiffness parameter of the Morse potential.

Although many parameters enter the Morse oscillator model, there are some clear qualitative features that emerge from the model which are of general nature. For example, the distance between the rainbow angles decreases with increasing angle of incidence as well as with increasing incident energy. This explains why many scattering experiments reveal only a single broad peak which is dominated by phonon scattering or other surface induced broadening. As a result, in these cases, one may ignore the corrugation taking into account only the surface motion.[43–45]

In this paper, we have limited the analysis to the angular distribution. The same expressions derived for the final joint angle and energy distribution as well as final average energy and its dependence on the scattering angle can be adapted also for the ratchet potentials considered in this paper. All that is needed is to add the relevant terms in the exponent. One may also use these expressions to estimate sticking probabilities and their dependence on the asymmetry.

Peskin and Moiseyev[54,55] and Hernandez *et al.*[56] predicted that a ratchetlike potential can induce an asymmetry in the angular distribution when flipping the crystal by 180° (or equivalently by changing the angle of incidence from θ_0 to $-\theta_0$). Such an asymmetry may also be found from the present theory; however this too will be dealt with in detail elsewhere.[53]

Finally, this paper was limited to two degrees of freedom, that is, to in-plane scattering. There is nothing in principle which limits the derivation; one can repeat the same reasoning allowing for the full three dimensional properties of the scattering problem to be taken into account. The only difficulty is that the resulting expressions do become more complicated.

ACKNOWLEDGMENT

We thank J. R. Manson for stimulating discussions and a critical reading of an early version of this manuscript. Stimulating discussions with W. Allison are gratefully acknowledged. We also thank the anonymous referees for their helpful comments. This work was supported by a grant of the Israel Science Foundation. S.M.A. would like to thank the Ministry of Science and Innovation of Spain for a project with Reference No. FIS2007-62006.

APPENDIX A: ENERGY LOSSES AND MOMENTUM CHANGES IN THE PRESENCE OF FRICTION

The derivation follows closely a similar derivation provided in Ref. 42. The central difference is that here the cor-

rugation potential is a sum of two terms, resulting from the addition of the second Fourier component to the corrugation potential. Details of the derivation are given in Ref. 42; here we provide the final results which are important for the actual application of the theory. The final momentum in the horizontal direction is given by the expression

$$\begin{aligned} p_x(t_0) &\simeq p_x - p_{z0}\left[K_1 \cos\left(\frac{2\pi}{l}x(0)\right) + K_2 \cos\left(\frac{4\pi}{l}x(0)\right)\right] \\ &\quad + \Delta p_{x,1} + \Delta p_{x,2} \\ &\equiv p_x + \delta p_x. \end{aligned} \tag{A1}$$

Comparing to the previous result in the absence of friction, we note that the coupling to the phonon bath induces a frictional momentum shift $\Delta p_{x,1}$ and a noise induced momentum shift $\Delta p_{x,2}$. The frictional momentum shift is (after an integration by parts)

$$\Delta p_{x,1} = -\eta_x \frac{p_x}{2} \int_{-t_0}^{t_0} dt g^2(z_t), \tag{A2}$$

and the noise induced momentum shift is

$$\begin{aligned} \Delta p_{x,2} &= \sqrt{M}\left\{\cos\left[\frac{2\pi}{l}x(t_0)\right]\sum_{j=1}^{N} c_{j_x} X_{jc} x_{j_x}(t_0) \right. \\ &\quad \left. + \sin\left[\frac{2\pi}{l}x(t_0)\right]\sum_{j=1}^{N} c_{j_x}\frac{X_{js}}{\omega_{j_x}} p_{j_x}(t_0)\right\} \\ &\equiv \cos\left[\frac{2\pi}{l}x(t_0)\right]\Delta p_{x,2c} + \sin\left[\frac{2\pi}{l}x(t_0)\right]\Delta p_{x,2s} \end{aligned} \tag{A3}$$

with

$$X_{jc} = \int_{-t_0}^{t_0} dt g(z_t)\left[\cos\left(\frac{2\pi}{l}\frac{p_x}{M}t\right)\right]\cos(\omega_{j_x} t), \tag{A4}$$

$$X_{js} = -\int_{-t_0}^{t_0} dt g(z_t)\sin\left(\frac{2\pi}{l}\frac{p_x}{M}t\right)\sin(\omega_{j_x} t), \tag{A5}$$

where

$$x_{j_x}(t_0) = x_{j_x}\cos[\omega_{j_x} t_0] + \frac{p_{j_x}}{\omega_{j_x}}\sin[\omega_{j_x} t_0], \tag{A6}$$

$$p_{j_x}(t_0) = -x_{j_x}\omega_{j_x}\sin[\omega_{j_x} t_0] + p_{j_x}\cos[\omega_{j_x} t_0], \tag{A7}$$

$$x(t_0) = x + \frac{p_x}{M}t_0. \tag{A8}$$

The average energy loss to the bath due to the motion in the x direction[42,48] is

$$\langle \Delta E_B\rangle_x = \Delta\epsilon - \cos\left(\frac{4\pi}{l}x(t_0)\right)\Delta\epsilon_x, \tag{A9}$$

where

$$\Delta\epsilon = E_0 \sin^2(\theta_{i0})\eta_x \int_{-t_0}^{t_0} dt\left\{g^2(z_t) + \frac{1}{\omega_x^2}\left[\frac{dg(z_t)}{dt}\right]^2\right\} \tag{A10}$$

and

$$\begin{aligned} \Delta\epsilon_x &= E_0 \sin^2(\theta_{i0})\eta_x \int_{-t_0}^{t_0} dt \cos(2\omega_x t) \\ &\quad \times\left\{g^2(z_t) + \frac{1}{\omega_x^2}\left[\frac{dg(z_t)}{dt}\right]^2\right\}. \end{aligned} \tag{A11}$$

The fluctuational energy loss in the horizontal direction is

$$\begin{aligned} \delta E_{B_x} &= \sqrt{M}\frac{l}{2\pi}\left\{\sin\left[\frac{2\pi}{l}x(t_0)\right]\sum_{j=1}^{N} c_{j_x} X_{jc} p_{j_x}(t_0) \right. \\ &\quad \left. + \cos\left[\frac{2\pi}{l}x(t_0)\right]\sum_{j=1}^{N} c_{j_x} X_{js}\omega_{j_x} x_{j_x}(t_0)\right\} \\ &\equiv \sin\left[\frac{2\pi}{l}x(t_0)\right]\delta E_{B_x s} + \cos\left[\frac{2\pi}{l}x(t_0)\right]\delta E_{B_x c}. \end{aligned} \tag{A12}$$

The average energy loss to the bath due to the vertical motion is (note that the dimension of η_x is time^{-1} while that of η_z is time^3/mass^2)

$$\langle \Delta E_B\rangle_z = M\eta_z \int_{-t_0}^{t_0} dt\left(\frac{d\bar{V}'(z_t)}{dt}\right)^2 \equiv -\frac{p_z \Delta p_{z,1}}{M}, \tag{A13}$$

and the associated fluctuational energy loss is

$$\delta E_{B_z} = -\sqrt{M}\sum_{j=1}^{N}\frac{c_{j_z}}{\omega_{j_z}} Z_{js} p_{j_z}(t_0) \equiv -\frac{p_z \Delta p_{z,2}}{M} \tag{A14}$$

with

$$Z_{js} = \int_{-t_0}^{t_0} dt \frac{d\bar{V}'(z_{t+t_0})}{dt}\sin(\omega_{j_z} t). \tag{A15}$$

APPENDIX B: ANALYTIC RESULTS FOR THE MORSE OSCILLATOR MODEL

Using the integrals specified in Sec. IV A one readily finds (using Maple software) that the energy loss in the vertical direction is

$$\langle \Delta E_B \rangle_z = \frac{4M\eta_z \Omega \alpha^2 V_0^2}{15}\left(\frac{(\cos^4(\Phi)+28\cos^2(\Phi)+16)-15\Phi\cot(\Phi)[2+\cos^2(\Phi)]}{\cos^4(\Phi)}\right). \tag{B1}$$

Similarly, using the coupling function $g(z)$ as given in Eq. (4.14) we find the following results:

$$\frac{\Delta p_{x,1}}{p_x} = -\frac{\eta_x \sin^2(\Phi)}{\Omega}\left(\frac{11\cos^2(\Phi)+4-3\Phi\cot(\Phi)[2\cos^2(\Phi)+3]}{6\cos^4(\Phi)}\right), \tag{B2}$$

$$G \equiv \Omega\int_{-\infty}^{\infty} dt g^2(z_t)\cos(2\omega_x t)$$

$$= \frac{2\pi\sin^2(\Phi)\sinh(2\bar{\Omega}\Phi)}{3\cos^4(\Phi)\sinh(2\bar{\Omega}\pi)}\cdot\left[\coth(2\bar{\Omega}\Phi)(4\bar{\Omega}^3\sin^2(\Phi)+\bar{\Omega}(11\cos^2(\Phi)+4))-6\bar{\Omega}^2\sin(2\Phi)-\cot(\Phi)\left(3\cos^2(\Phi)+\frac{9}{2}\right)\right], \tag{B3}$$

$$\Delta\epsilon = \frac{M\bar{\Omega}^2\eta_x\Omega l^2}{24\pi^2}\sin^2(\Phi)\left(\frac{11\cos^2(\Phi)+4-3\Phi\cot(\Phi)[2\cos^2(\Phi)+3]}{\cos^4(\Phi)}\right)$$
$$+\frac{M\eta_x\Omega l^2}{120\pi^2}\left(\frac{6\cos^4(\Phi)+83\cos^2(\Phi)+16-15\Phi\cot(\Phi)[4\cos^2(\Phi)+3]}{\cos^4(\Phi)}\right), \tag{B4}$$

$$\Delta\epsilon_x = \frac{M\eta_x\Omega l^2}{60\pi\cos^4(\Phi)\sinh(2\bar{\Omega}\pi)}\cosh(2\bar{\Omega}\Phi)\cdot(4\bar{\Omega}^5\sin^4(\Phi)+\bar{\Omega}^3\sin^2(\Phi)[35\cos^2(\Phi)+20]+\bar{\Omega}[6\cos^4(\Phi)+83\cos^2(\Phi)+16])$$
$$-\frac{M\eta_x\Omega l^2}{24\pi\cos^3(\Phi)\sinh(2\bar{\Omega}\pi)}\sinh(2\bar{\Omega}\Phi)\cdot\left(8\bar{\Omega}^4\sin^3(\Phi)+\bar{\Omega}^2\sin(\Phi)[10\cos^2(\Phi)+29]+3\frac{4\cos^2(\Phi)+3}{\sin(\Phi)}\right). \tag{B5}$$

These analytic results are all that is needed to compute the angular shift of Eq. (3.18); the variance as given in Eq. (3.17) and thus the angular distribution as given in Eq. (3.16). Only the remaining integration over the horizontal coordinate needs to be carried out numerically.

*eli.pollak@weizmann.ac.il

[1] V. Bortolani and A. C. Levi, Riv. Nuovo Cimento **9**, 1 (1986).
[2] D. Farias and K.-H. Rieder, Rep. Prog. Phys. **61**, 1575 (1998).
[3] B. Gumhalter, Phys. Rep. **351**, 1 (2001).
[4] R. Guantes, A. S. Sanz, J. Margalef-Roig, and S. Miret-Artés, Surf. Sci. Rep. **53**, 199 (2004).
[5] A. S. Sanz and S. Miret-Artés, Phys. Rep. **451**, 37 (2007).
[6] J. R. Manson, in *Handbook of Surface Science*, edited by N. V. Richardson and S. Holloway, Vol. 3 Surface Dynamics, edited by E. Hasselbrink and B. Lundqvist (Elsevier, Amsterdam, 2008).
[7] A. Bellman, A. Morgante, M. Polli, F. Tommasini, D. Cvetko, V. R. Dhanak, A. Lausi, K. C. Prince, and R. Rosei, Surf. Sci. **298**, 1 (1993).
[8] A. Šiber and B. Gumhalter, Prog. Surf. Sci. **74**, 375 (2003).
[9] G. Bracco, P. Cantini, E. Cavanna, R. Tartarek, and A. Glachant, Surf. Sci. **136**, 169 (1984).
[10] P. Cortona, M. G. Dondi, and F. Tommasini, Surf. Sci. **261**, L35 (1992).
[11] S. Yamamoto and R. Stickney, J. Chem. Phys. **53**, 1594 (1970).
[12] K. H. Rieder and W. Stocker, Phys. Rev. B **31**, 3392 (1985).
[13] R. M. Aten, D. Blanchard, L. R. Allen, E. R. Conrad, M. Nelson, and T. Engel, Surf. Sci. **183**, 515 (1987).
[14] M. E. M. Spruit, E. W. Kuipers, M. G. Tenner, J. Kimman, and A. W. Kleyn, J. Vac. Sci. Technol. A **5**, 496 (1987).
[15] H. P. Steinrück and R. J. Madix, Surf. Sci. **185**, 36 (1987).
[16] G. Vidali, C. W. Hutchings, and M. Karimi, Surf. Sci. **202**, L595 (1988).
[17] C. T. Rettner, E. K. Schweizer, and C. B. Mullins, J. Chem. Phys. **90**, 3800 (1989).
[18] E. K. Schweizer and C. T. Rettner, Phys. Rev. Lett. **62**, 3085 (1989).
[19] H. F. Winters, H. Coufal, C. T. Rettner, and D. S. Bethune, Phys. Rev. B **41**, 6240 (1990).
[20] M. Head-Gordon, J. C. Tully, H. Schliching, and D. Menzel, J. Chem. Phys. **95**, 9266 (1991).
[21] E. K. Schweizer, C. T. Rettner, and S. Holloway, Surf. Sci. **249**, 335 (1991).
[22] R. J. W. E. Lahaye, A. W. Kleyn, S. Stolte, and S. Holloway, Surf. Sci. **338**, 169 (1995).
[23] A. Raukema, R. J. Dirksen, and A. W. Kleyn, J. Chem. Phys. **103**, 6217 (1995).
[24] R. J. W. E. Lahaye, S. Stolte, S. Holloway, and A. W. Kleyn, Surf. Sci. **363**, 91 (1996).

[25] B. Berenbak, S. Zboray, B. Riedmuller, D. C. Papageorgopoulos, S. Stolte, and A. W. Kleyn, Phys. Chem. Chem. Phys. **4**, 68 (2002).
[26] K. D. Gibson, N. Isa, and S. J. Sibener, J. Chem. Phys. **119**, 13083 (2003).
[27] H. Castejón, Surf. Sci. **564**, 165 (2004).
[28] T. Kondo, H. S. Kato, T. Yamada, S. Yamamoto, and M. Kawai, Eur. Phys. J. D **38**, 129 (2006).
[29] K. D. Gibson, S. J. Sibener, H. P. Upadhyaya, A. L. Brunsvold, J. Zhang, T. K. Minton, and D. Troya, J. Chem. Phys. **128**, 224708 (2008).
[30] A. G. Stoll, D. L. Smith, and R. P. Merrill, J. Chem. Phys. **54**, 163 (1971).
[31] A. Amirav, M. J. Cardillo, P. L. Trevor, C. Lim, and J. C. Tully, J. Chem. Phys. **87**, 1796 (1987).
[32] C. T. Rettner, J. A. Barker, and D. S. Bethune, Phys. Rev. Lett. **67**, 2183 (1991).
[33] J. A. Barker, C. T. Rettner, and D. S. Bethune, Chem. Phys. Lett. **188**, 471 (1992).
[34] S. Schroeder, M. C. McMaster, J. A. Stinnett, and R. J. Madix, Surf. Sci. Lett. **297**, L148 (1993).
[35] M. D. Ellison, C. M. Matthews, and R. N. Zare, J. Chem. Phys. **112**, 1975 (2000).
[36] Y. Watanabe, H. Yamaguchi, H. Hashinokuchi, K. Sawabe, S. Maruyama, Y. Matsumoto, and K. Shobatake, Chem. Phys. Lett. **413**, 331 (2005).
[37] Y. Watanabe, H. Yamaguchi, H. Hashinokuchi, K. Sawabe, S. Maruyama, Y. Matsumoto, and K. Shobatake, Eur. Phys. J. D **38**, 103 (2006).
[38] J. C. Tully, J. Chem. Phys. **92**, 680 (1990).
[39] A. W. Kleyn and T. C. M. Horn, Phys. Rep. **199**, 191 (1991).
[40] T. Yan, W. L. Hase, and J. C. Tully, J. Chem. Phys. **120**, 1031 (2004).
[41] E. Pollak, S. Sengupta, and S. Miret-Artés, J. Chem. Phys. **129**, 054107 (2008).
[42] E. Pollak and S. Miret-Artés, J. Chem. Phys. **130**, 194710 (2009).
[43] J. R. Manson, Phys. Rev. B **43**, 6924 (1991).
[44] J. R. Manson, V. Celli, and D. Himes, Phys. Rev. B **49**, 2782 (1994).
[45] W. W. Hayes and J. R. Manson, J. Chem. Phys. **127**, 164714 (2007).
[46] J. N. Smith, D. R. O'Keefe, and R. L. Palmer, J. Chem. Phys. **52**, 315 (1970).
[47] T. Engel and J. H. Weare, Surf. Sci. **164**, 403 (1985).
[48] E. Pollak, H. Grabert, and P. Hänggi, J. Chem. Phys. **91**, 4073 (1989).
[49] J. R. Klein and M. W. Cole, Surf. Sci. Lett. **81**, L319 (1979).
[50] Y. Ekinci and J. P. Toennies, Surf. Sci. **563**, 127 (2004).
[51] P. S. Weiss, A. Amirav, P. L. Trevor, and M. J. Cardillo, J. Vac. Sci. Technol. A **6**, 889 (1988).
[52] G. Vidali, G. Ihm, H.-Y. Kim, and M. W. Cole, Surf. Sci. Rep. **12**, 135 (1991).
[53] S. Miret-Artés and E. Pollak (unpublished).
[54] U. Peskin and N. Moiseyev, J. Chem. Phys. **97**, 2804 (1992).
[55] U. Peskin and N. Moiseyev, Int. J. Quantum Chem. **46**, 343 (1993).
[56] M. Hernández, S. Miret-Artés, P. Villarreal, and G. Delgado-Barrio, Surf. Sci. Lett. **290**, L693 (1993).